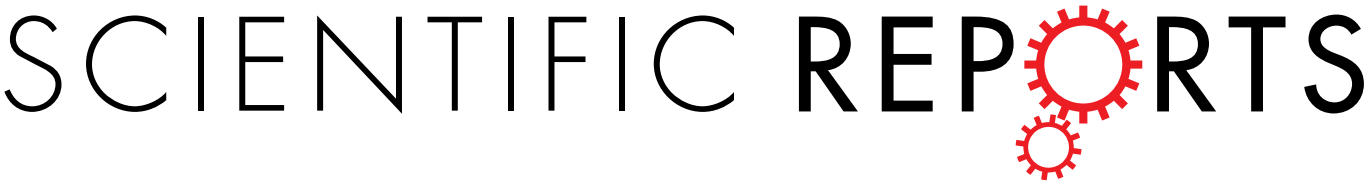

OPEN

Surface modification of layered perovskite Sr_2TiO_4 for improved CO_2 photoreduction with H_2O to CH_4

Received: 6 June 2017
Accepted: 10 November 2017
Published online: 27 November 2017

Byeong Sub Kwak[1], Jeong Yeon Do[1], No-Kuk Park[2] & Misook Kang[1]

Layered perovskite Sr_2TiO_4 photocatalyst was synthesized by using sol-gel method with citric acid. In order to increase the surface area of layered perovskite Sr_2TiO_4, and thus to improve its photocatalytic activity for CO_2 reduction, its surface was modified via hydrogen treatment or exfoliation. The physical and chemical properties of the prepared catalysts were characterized by X-ray diffraction, high-resolution transmission electron microscopy, elemental mapping analysis, energy-dispersive X-ray spectroscopy, N_2 adsorption-desorption, UV-Vis spectroscopy, X-ray photoelectron spectroscopy, photoluminescence, and electrophoretic light scattering. CO_2 photoreduction was performed in a closed reactor under 6 W/cm^2 UV irradiation. The gaseous products were analyzed using a gas chromatograph equipped with flame ionization and thermal conductivity detectors. The exfoliated Sr_2TiO_4 catalyst (E-Sr_2TiO_4) exhibited a narrow band gap, a large surface area, and high dispersion. Owing to these advantageous properties, E-Sr_2TiO_4 photocatalyst showed an excellent catalytic performance for CO_2 photoreduction reaction. The rate of CH_4 production from the photoreduction of CO_2 with H_2O using E-Sr_2TiO_4 was about 3431.77 μmol/g_{cat} after 8 h.

As is well known, the temperature of Earth is increasing owing to greenhouse gas emissions, and CO_2 makes up the largest portion of these greenhouse gases. The United Nations Framework Convention on Climate Change (UNFCCC) has concluded that, to maintain a stable environmental, global warming since industrialization must not exceed 2 °C. However, according to their investigation, the average ground temperature since industrialization has already increased by 0.75 °C. When we consider the heat absorbed by the sea, this temperature increases by a further 0.6 °C. Consequently, we have a temperature increase of only 0.65 °C until the temperature change set by the UNFCCC is already reached. Because of the global warming, various natural disasters have been occurred[1]. In order to avoid this problem, we must reduce CO_2 emissions. However, it is impossible to stop CO_2 emissions completely because of the current industrial systems are depending on the fossil fuels.

Carbon capture and storage (CCS) technology has been developed in order to reduce and/or control the CO_2 emissions[2,3]. However, this CCS technology has several problems such as high cost, additional energy requirements, stability, and storage limitations. Therefore, carbon capture and utilization (CCU) technology is expected to replace it[4–6], and is advantageous in economic and environmental view because it can prevent CO_2 emissions, and convert them into useful materials. There are various strategies for CO_2 utilization. One is the non-conversional use of CO_2, and the others involve its conversion using chemical, biochemical, photochemical, and electrochemical methods. Of these, the photochemical method is a more promising technology in environmental terms. CO_2 photoreduction using a photocatalyst can generate useful compounds such as CH_4, HCOOH, HCHO, and CH_3OH[7]. Much research has been devoted to this field since the first report by Inoue *et al.*[8] on the photoreduction of CO_2, and many different semiconductors have been developed and used as photocatalysts, such as TiO_2[9], WO_3[10], ZnO[11], GaP[12], CdS[13], and SiC[14]. Of these, TiO_2 is one of the most well-known and widely used materials. In order to improve the optical properties of TiO_2, it has been combined with various metals to form hybridized composites such as Ag/TiO_2[15], Pt/TiO_2[16], Ru/TiO_2[17], Pd/TiO_2[18], Ni/TiO_2[19], Cu/TiO_2[20], TiO_2/Cu-TiO_2[21], CeO_2-TiO_2[22], MgO-TiO_2[23], NiO-In_2O_3/TiO_2[24], CuS_x-TiO_2[25], NiS-TiO_2[26], In_2O_3/TiO_2[27], TiO_2/Fe-TiO_2[28]

[1]Department of Chemistry, College of Natural Sciences, Yeungnam University, Gyeongsan, Gyeongbuk, 38541, Republic of Korea. [2]School of Chemical Engineering, Yeungnam University, Gyeongsan, Gyeongbuk, 38541, Republic of Korea. Correspondence and requests for materials should be addressed to M.K. (email: mskang@ynu.ac.kr)

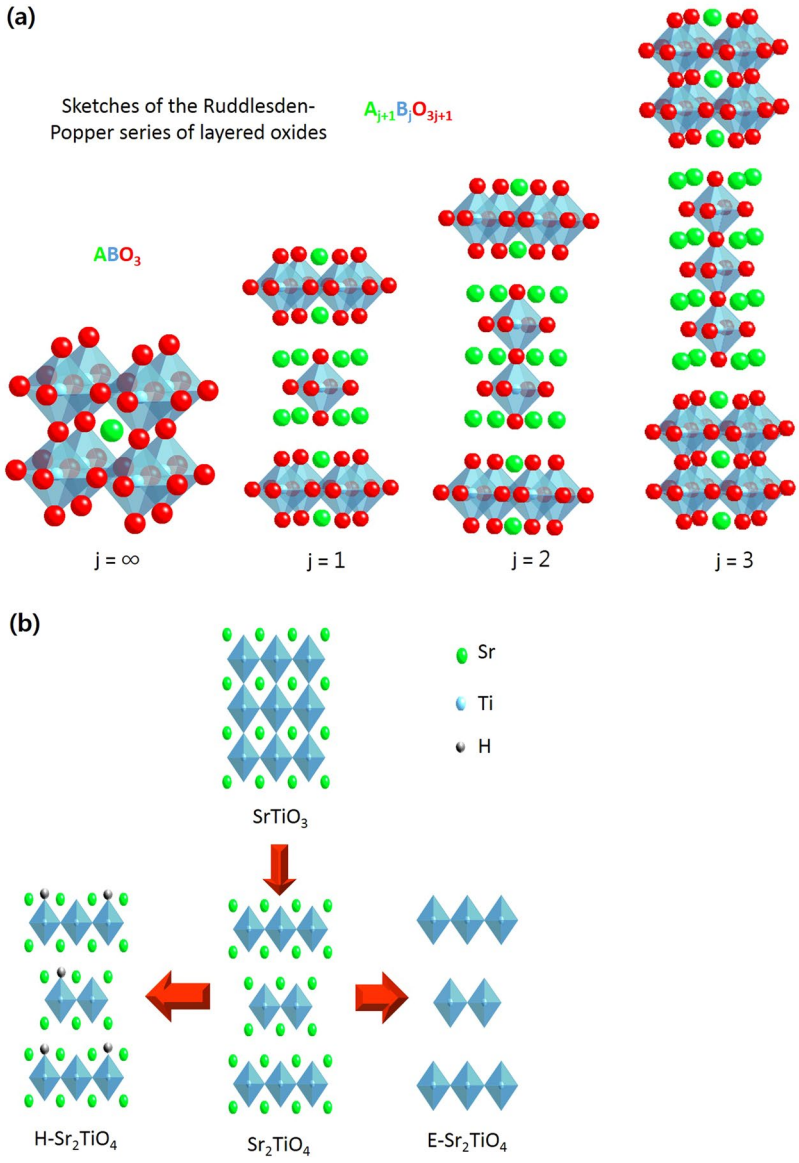

Figure 1. (**a**) Ruddlesden-Popper phase of layered oxide and (**b**) the overview of catalyst surface modification.

and multi-walled carbon nanotube (MWCNT)@TiO_2[29] in an attempt to reduce the band gap or suppress recombination of photogenerated charge carriers. Also, catalysts having a combination of an organic and metal material such as g-C_3N_4[30], $Ni_{12}P_5$/g-C_3N_4[31], Au cluster-NP/C_3N_4[32], AgX/g-C_3N_4 (X = Cl and Br)[33], RuRu′/Ag/NS-C_3N_4[34–37] and Co-ZIF[38–41] are being developed.

Recently, the development of TiO_2 photocatalysts with the perovskite structure ABO_3, has attracted due to the unique perovskite structure, their composition can be easily changed at the A, and B sites and the metal introduced can be quantitatively substituted into the skeleton. Among the perovskite semiconductors, $SrTiO_3$ is widely used as a photocatalyst. Much like TiO_2, $SrTiO_3$ has been combined with other species to form hybrid composites such as Mn/$SrTiO_3$[42], Cu/$SrTiO_3$[43], N-doped TiO_2-$SrTiO_3$[44], Fe_2O_3/$SrTiO_3$[45], $SrTiO_3$:Cr/Ta/F[46], $SrTiO_3$/HZSM-5[47], $SrTiO_3$/TiO_2/H-titanate nanofiber[48], $SrTiO_3$:Rh/Sb[49], La/Cr-doped $SrTiO_3$[50], Pt/$SrTiO_3$[51], Zn/$SrTiO_3$[52], Ag_3PO_4/Cr-$SrTiO_3$[53], and g-C_3N_4-$SrTiO_3$:Rh[54] to improve its photocatalytic performance. Studies on other perovskite catalysts, including $Ca_xTi_yO_3$[55], and basalt fiber@$PbTiO_3$[56], also have been recently reported.

Another advantage of perovskite is that it forms a layered perovskite depending on the nature and contents of the A and B ions. Figure 1a shows the structure of a Ruddlesden-Popper $A_{j+1}B_jO_{3j+1}$ perovskite. Here, when the j value increases, the structure tends towards an ABO_3 perovskite. In particular, A_2BO_4, for which j = 1, shows a layered structure with a large gap between each BO_6 octahedron.

In this study, we have attempted to improve the photocatalytic performance of Sr_2TiO_4 layered perovskite by increasing its surface area (Fig. 1b). The surface of the synthesized catalyst was hydrogen treated or exfoliated to increase its interaction with the CO_2 feed material and thus amplify its CO_2 photoreduction activity. The characteristic properties of the synthesized catalysts were measured by using a variety of techniques such as using X-ray

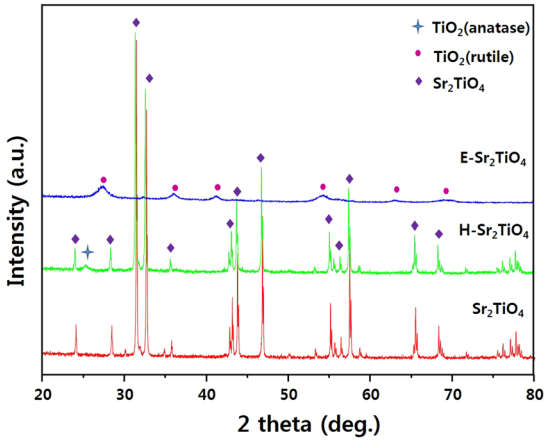

Figure 2. XRD patterns of Sr_2TiO_4, H-Sr_2TiO_4 and exfoliation Sr_2TiO_4 catalysts.

diffraction (XRD), high-resolution transmission electron microscopy (HR-TEM), N_2 adsorption-desorption isotherm analysis, UV-Vis spectroscopy, photoluminescence (PL), zeta potential analysis, and X-ray photoelectron spectroscopy (XPS). Furthermore, their photocatalytic activity for the reduction of CO_2 with H_2O under UV light was studied.

Results

X-ray diffraction (XRD) patterns. The XRD patterns for Sr_2TiO_4, H-Sr_2TiO_4, and E-Sr_2TiO_4 are given in Fig. 2. The peaks for Sr_2TiO_4 are observed at $2\theta = 24.076$, 28.386, 31.464, 32.656, 35.673, 42.899, 43.217, 43.852, 46.791, 55.049, 55.605, 56.319, 57.431, 65.452, and 68.390°, which are assigned to the (011), (004), (013), (110), (112), (015), (006), (114), (020), (116), (024), (017), (123), (026), and (220) planes of Sr_2TiO_4, respectively, identifying it as a layered perovskite-type tetragonal structure (JCPDS 00-039-1471)[57]. The crystallite size of Sr_2TiO_4 calculated using Scherer's equation based on the (013) plane is 12.856 Å[58]. After hydrogen treatment, an anatase TiO_2 peak is observed at $2\theta = 25.429°$. However, the other peaks for the Sr_2TiO_4 structure are maintained, and the crystallite sizes based on the Sr_2TiO_4 (013) plane and the TiO_2 anatase (011) plane are 9.371 and 3.024 Å, respectively. Conversely, the Sr_2TiO_4 sample exfoliated with HNO_3 and TPAOH presents a different XRD pattern. The peaks for E-Sr_2TiO_4 are found at 27.141, 36.070, 41.232, 54.414, 63.069, and 69.105°, which are assigned to the (110), (011), (111), (121), (130), and (031) planes of rutile TiO_2, respectively[59]. These structural changes are due to the fact that the Sr ions located between the Sr_2TiO_4 layers are removed by HNO_3 treatment, and only the TiO_6 octahedra (corresponding to BO_6) remain. The crystal structure analysis reveals that the Ti forms a rutile structure in the Sr_2TiO_4 and that the Sr is intercalated between the layers. The crystallite size of the catalysts was calculated using scherrer's equation. In the case of Sr_2TiO_4 and H-Sr_2TiO_4, (013) plane was selected, and (110) plane was selected for E-Sr_2TiO_4. As a result, the crystallite size of Sr_2TiO_4, H-Sr_2TiO_4, and E-Sr_2TiO_4 were found to be 11.568, 11.578, 1.165 Å, respectively.

High-resolution transmission electron microscopy (HR-TEM), element mapping and EDX analysis. The differences in the morphologies of Sr_2TiO_4 and E-Sr_2TiO_4 were investigated using HR-TEM and selected area electron diffraction (SAED) (Fig. 3). The larger particles are observed in Sr_2TiO_4, and whereas E-Sr_2TiO_4 consists of the particles form a separate sheets or randomly folded sheets. The images show that the interplanar distance for E-Sr_2TiO_4 is larger than that for Sr_2TiO_4. The d-spacings for the Sr_2TiO_4 (013) plane and the E-Sr_2TiO_4 (110) plane are 2.84 and 3.25 Å, respectively. These results are in accordance with the values derived from XRD patterns.

The compositions of Sr_2TiO_4 and E-Sr_2TiO_4 were analyzed by HR-TEM element mapping analysis and EDX, and the results are shown in Fig. 4 and Table 1. In Sr_2TiO_4, Sr and Ti ions are uniformly distributed throughout the particles and Sr ions are more abundant than Ti ions. The atomic percent values for Sr and Ti are 16 and 11%, respectively. However, the Sr ion content of E-Sr_2TiO_4 is much lower than that of Sr_2TiO_4. Furthermore, EDX analysis showed that the Sr ion content, which is about 1.4-times that of Ti in Sr_2TiO_4, is reduced to just 0.07% that of Ti in E-Sr_2TiO_4. Thus, these results support the assertion that the layers are separated because Sr ions are removed from the interlayers by exfoliation.

Brunaure-Emmett-Teller (BET) surface area analysis. Figure 5 shows the N_2 adsorption-desorption isotherms at 77 K for P-25, which was used as a comparative sample, Sr_2TiO_4, H-Sr_2TiO_4, and E-Sr_2TiO_4. According to the IUPAC classification, the adsorption-desorption isotherm curves of all the catalysts belong to type III. Therefore, the synthesized catalysts are non-porous materials. However, the slight hysteresis in the curves is due to the bulk pores between the particles. The specific surface areas of Sr_2TiO_4 and H-Sr_2TiO_4 are 1.19 and 0.78 m^2/g, respectively, which are very low. However, E-Sr_2TiO_4 has a specific surface area of 358.54 m^2/g, which is much larger than those of Sr_2TiO_4 and H-Sr_2TiO_4. The increase in the specific surface are of E-Sr_2TiO_4 is due not only to the removal of Sr ions from between the layers, but also to the separation of the layers, as shown in the HR-TEM images. The increase in catalyst surface area leads to an increase in the number of active sites for CO_2

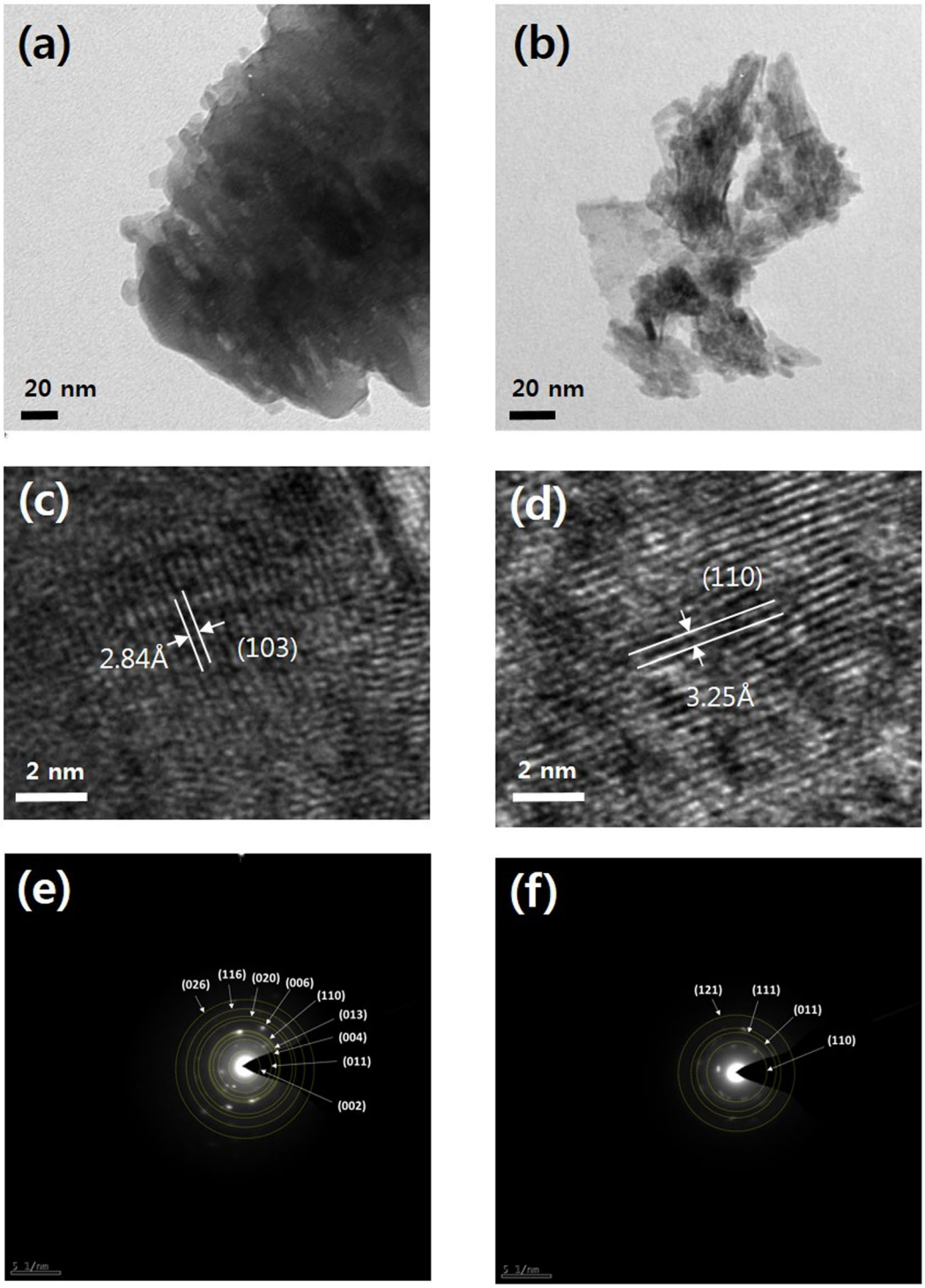

Figure 3. High resolution TEM and SAED images of catalysts: (**a**), (**c**) Sr_2TiO_4 and (**b**), (**d**) exfoliation Sr_2TiO_4.

and H_2O to react, leading to an increase in reactivity. Therefore, E-Sr_2TiO_4 was expected to exhibit improved catalytic activity compared to those of Sr_2TiO_4 and H-Sr_2TiO_4. This specific surface area is considerably larger than that of the commercial catalyst P-25, which is 43.65 m^2/g.

Optical properties of photocatalysts. Figures 6 and 7 show the UV-Vis spectra and Tauc's plots of P-25, Sr_2TiO_4, H-Sr_2TiO_4, and E-Sr_2TiO_4. The UV absorptions of Sr_2TiO_4 and H-Sr_2TiO_4 are blue-shifted compared to that of P-25 because of the influence of SrO, with its band gap of 5.71 eV[60]. Conversely, the absorbance of E-Sr_2TiO_4 is shifted to a longer wavelength due to the removal of Sr ions. Most interestingly, it moved to longer wavelength than that of P-25. This is because E-Sr_2TiO_4 has a rutile TiO_2 structure (band gap: 3.0 eV), as

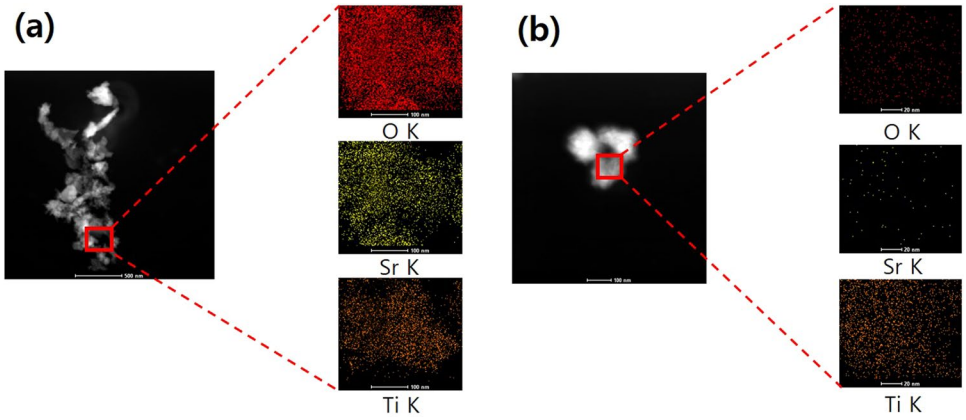

Figure 4. HR-TEM elemental mapping analysis of catalysts: (**a**) Sr_2TiO_4 and (**b**) exfoliation Sr_2TiO_4.

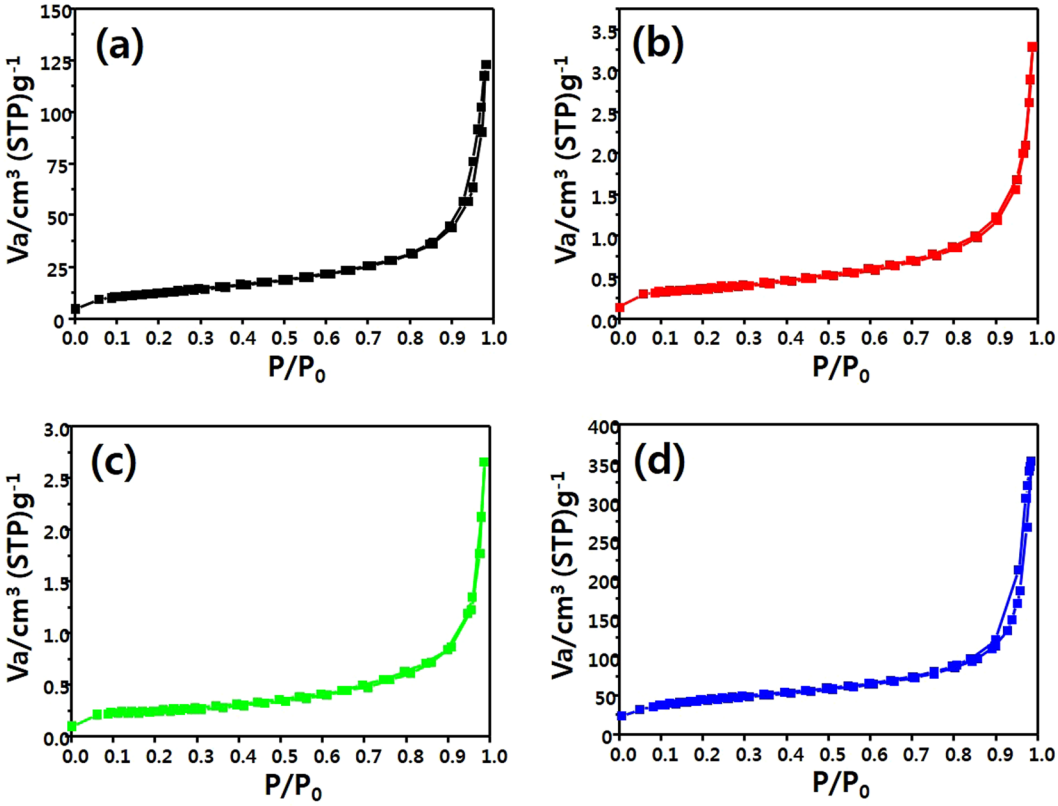

Figure 5. N_2 adsorption and desorption isotherms of catalysts; (**a**) P-25, (**b**) Sr_2TiO_4, (**c**) H-Sr_2TiO_4 and (**d**) E-Sr_2TiO_4.

Catalyst	(Atomic %)		
	Sr	Ti	O
Sr_2TiO_4	16.16	11.93	71.89
E-Sr_2TiO_4	4.80	68.29	26.90

Table 1. Atomic ratio by HR-TEM EDX analysis.

confirmed by the XRD analysis above. Therefore, the absorbance of E-Sr_2TiO_4 is shifted to longer wavelength than that of P-25, which composed mainly of anatase TiO_2 (band gap: 3.2 eV). The band gap was calculated using the Tauc equation[61]:

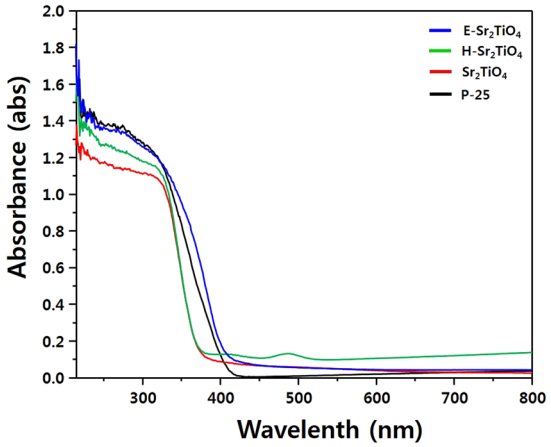

Figure 6. UV-visible spectra of catalysts.

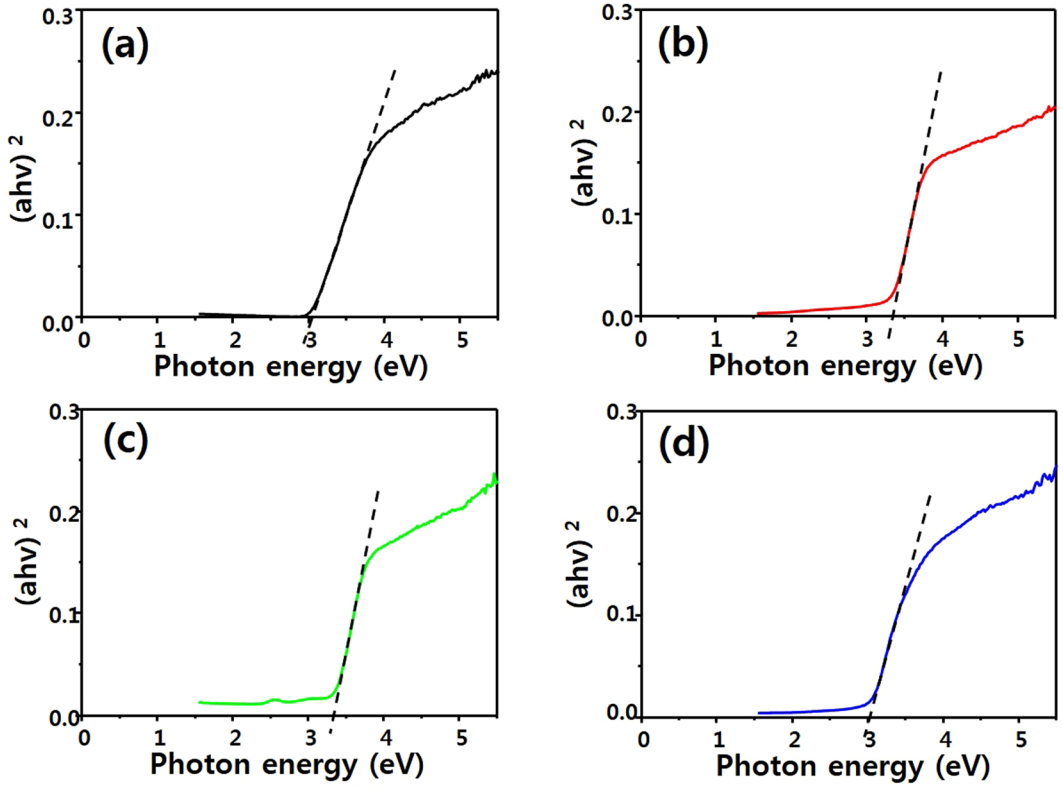

Figure 7. Tauc plot of catalysts; (**a**) P-25, (**b**) Sr_2TiO_4, (**c**) H-Sr_2TiO_4 and (**d**) E-Sr_2TiO_4.

$$\alpha h\nu = A(h\nu - E_{bg})^{1/2} \quad (1)$$

where α, h, ν, A, and E_{bg} represent the absorption coefficient, Plank's constant, light frequency, a constant, and band gap energy, respectively. In a plot of $(\alpha h\nu)^2$ versus photon energy ($h\nu$), the intercept on the x axis gives the band gap. Using this method, the band gap of P-25, Sr_2TiO_4, H-Sr_2TiO_4 and E-Sr_2TiO_4 were calculated to be 3.16, 3.33, 3.34, and 3.03 eV, respectively. Therefore, E-Sr_2TiO_4 has the narrowest band gap, making it most suitable as a photocatalyst.

Photocatalysts with narrower band gaps have advantages in terms of photosensitization. However, in order to exhibit good performance in the current system, the band gap of a photocatalyst should also include the CO_2/CH_4 and H_2O/O_2 reduction potentials. Figure 8 shows the XPS valance band spectra of the catalysts. Based on the data obtained, the valance band value of the catalysts was confirmed, and the values for P-25, Sr_2TiO_4, H-Sr_2TiO_4, and E-Sr_2TiO_4 are 2.46, 2.34, 1.60, and 2.06 eV, respectively. When the vacuum level of 4.5 eV is corrected to 0 V for a standard hydrogen electrode (SHE) and the work function of the XPS instrument is taken as 4.62 eV[62],

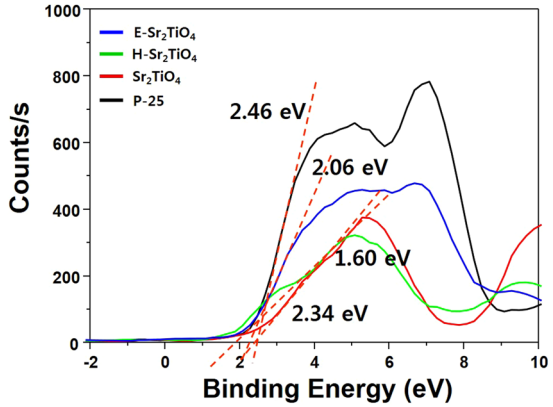

Figure 8. XPS valance band spectra of catalysts.

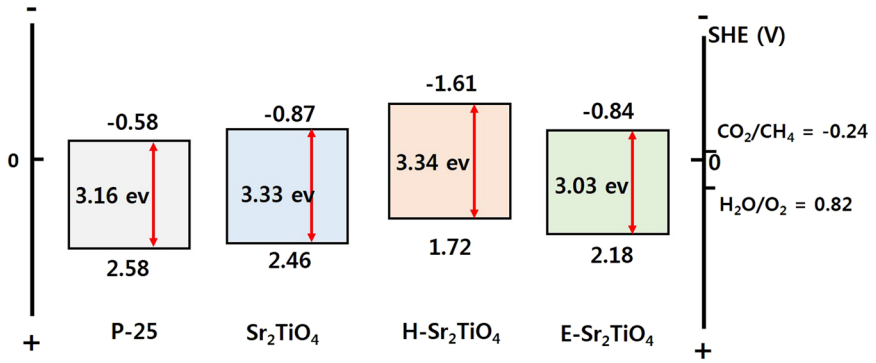

Figure 9. Energy diagram of catalysts.

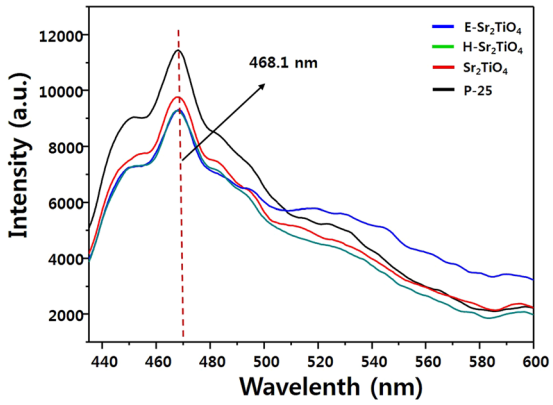

Figure 10. PL emission spectra of catalysts.

the valance band maximum values for P-25, Sr_2TiO_4, H-Sr_2TiO_4 and E-Sr_2TiO_4 are 2.58, 2.46, 1.72 and 2.18 eV (vs. SHE), respectively. According to these valance band and band gap values, the conduction band minimum values for P-25, Sr_2TiO_4, H-Sr_2TiO_4, and E-Sr_2TiO_4 are −0.58, 0.87, −1.61, and −0.84 eV (vs. SHE), respectively. Figure 9 shows the energy diagrams obtained for the catalysts using the valance and conduction band values and the band gap. All catalysts contain the CO_2/CH_4 and H_2O/O_2 reduction potential. Therefore, the synthesized catalysts are suitable for the photoreduction of CO_2 with H_2O to CH_4.

In order to understand the recombination of excited electrons and holes, PL analysis was conducted, and the results are shown in Fig. 10. The PL spectra of the catalysts show a strong emission signal at 468.1 nm. The PL intensity of Sr_2TiO_4 is smaller than that of P-25. This is due to a decrease in the number of excited electrons because of the wide band gap of Sr_2TiO_4. The intensity for H-Sr_2TiO_4 is lower than that of Sr_2TiO_4. This is because the oxidation state of the exposed Ti on the surface is reduced to $(4\text{-}\delta)^+$, which is not +4, and the reduced Ti

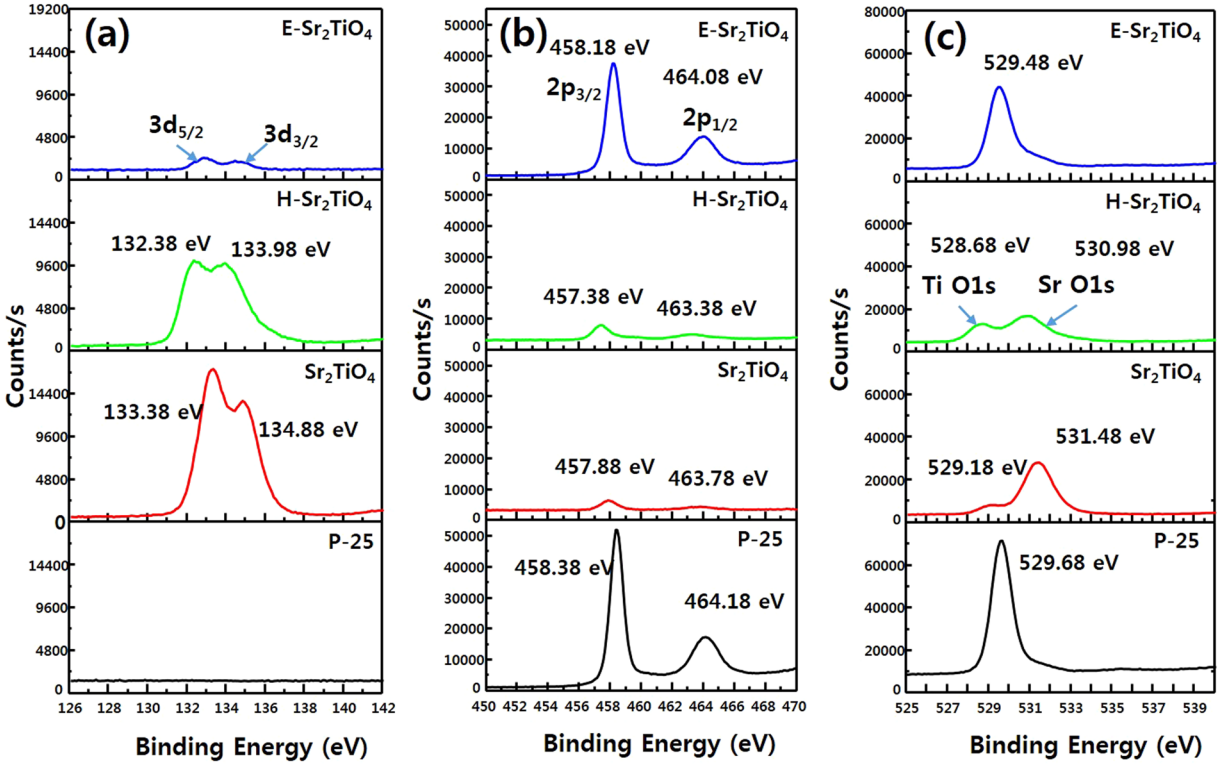

Figure 11. XPS spectra of catalysts; (**a**) Sr 3d spectra, (**b**) Ti 2p spectra, and (**c**) O 1s spectra.

suppresses the recombination of electrons and holes by trapping the excited electrons in the conduction band. The E-Sr_2TiO_4 also exhibits a PL intensity lower than that of Sr_2TiO_4 and much lower than that of P-25. Generally, excited electrons and holes move from the bulk of a particle to its surface where they react with reactants. The recombination of excited electrons and holes takes place in the bulk or on the surface of a particle during transport. When the particles are exfoliated, the internal area of the particles decreases and the distance to the surface for the electrons and holes decreases. Therefore, recombination inside the particles is also reduced. This is the reason that E-Sr_2TiO_4 has a lower PL intensity than that of P-25. Thus, the above analysis indicates that H-Sr_2TiO_4 and E-Sr_2TiO_4 will be better photocatalysts than Sr_2TiO_4.

X-ray photoelectron spectroscopy (XPS) analysis. The XPS spectra of the photocatalysts were obtained to confirm the oxidation state of the elements according to their chemical bonding, and the results are shown in Fig. 11. For Sr_2TiO_4, the peaks located at 133.38 and 134.88 eV are assigned to Sr-$3d_{5/2}$ and Sr-$3d_{3/2}$ core levels respectively. In H-Sr_2TiO_4, the Sr 3d peaks are shifted toward a slightly lower binding energy. In E-Sr_2TiO_4, the intensity of the 3d peaks is greatly reduced. This is due to the removal of Sr ions from the interlayer spaces, as described above. The Ti $2p_{3/2}$ and $2p_{1/2}$ peaks of Sr_2TiO_4 are observed at 457.88 and 463.78 eV, respectively. The Ti 2p peaks for H-Sr_2TiO_4 are shifted to a lower binding energy, similarly to the Sr 3d peaks. This is because some of the Sr^{2+} and Ti^{4+} ions are reduced by hydrogen to $Sr^{(2-\delta)+}$ and $Ti^{(4-\delta)+}$, respectively. The Ti 2p peaks for E-Sr_2TiO_4 have significantly different peak intensities to Sr_2TiO_4 or H-Sr_2TiO_4, and its Ti $2p_{3/2}$ and Ti $2p_{1/2}$ peaks are observed at 458.18 and 464.08 eV, respectively. This binding energy is shifted slightly lower compared to that of P-25. Therefore, the Ti ions of E-Sr_2TiO_4 are slightly more reduced ions than in P-25. It is believed that this can induce vacancies in the crystal framework and facilitate the movement of electrons and holes, which can be advantageous for photocatalytic activity.

There are two O 1 s peaks in Sr_2TiO_4 and H-Sr_2TiO_4. The peak at ~529 eV is from oxygen bound to Ti, and the peak at ~531 eV corresponds to oxygen bound to Sr. For E-Sr_2TiO_4, only the peak corresponding to oxygen bonded to Ti is observed (at 529.48 eV), because the Sr is removed by exfoliation.

Zeta potential analysis of photocatalysts. Since the catalytic reaction takes place in H_2O, it is important to study the dispersion of the catalyst particles in H_2O. The zeta potentials were measured after dispersing the catalysts in distilled water or in bubbling-CO_2 solution (i.e., the reaction conditions), and the results are shown in Table 2. Generally, a larger absolute value for the measured zeta potential means that the particles are well dispersed in a solution. The zeta potentials for Sr_2TiO_4, H-Sr_2TiO_4, E-Sr_2TiO_4, and P-25 are −11.99, −11.15, −42.39, and −15.61 mV, respectively. Therefore, the degree of colloidal dispersion in H_2O follows the order E-Sr_2TiO_4 > P-25 > Sr_2TiO_4 > H-Sr_2TiO_4. Thus, all catalysts can be adequately dispersed in H_2O. However, the zeta potential shows a different pattern after CO_2 bubbling: all the negative potential values are changed to positive values. The zeta potentials for Sr_2TiO_4, H-Sr_2TiO_4, E-Sr_2TiO_4, and P-25 are 1.16, 16.29, 26.22, and 22.00 mV, respectively.

		P-25	Sr_2TiO_4	H-Sr_2TiO_4	E-Sr_2TiO_4
Band gap (eV)		3.16	3.33	3.34	3.03
S_{BET} (m^2/g)		43.65	1.19	0.78	358.54
Zeta potential (mV)	Before-CO_2	−15.61	−11.99	−11.15	−42.39
	After-CO_2	22.00	1.16	16.29	26.22

Table 2. Summary of physical and chemical properties of catalysts.

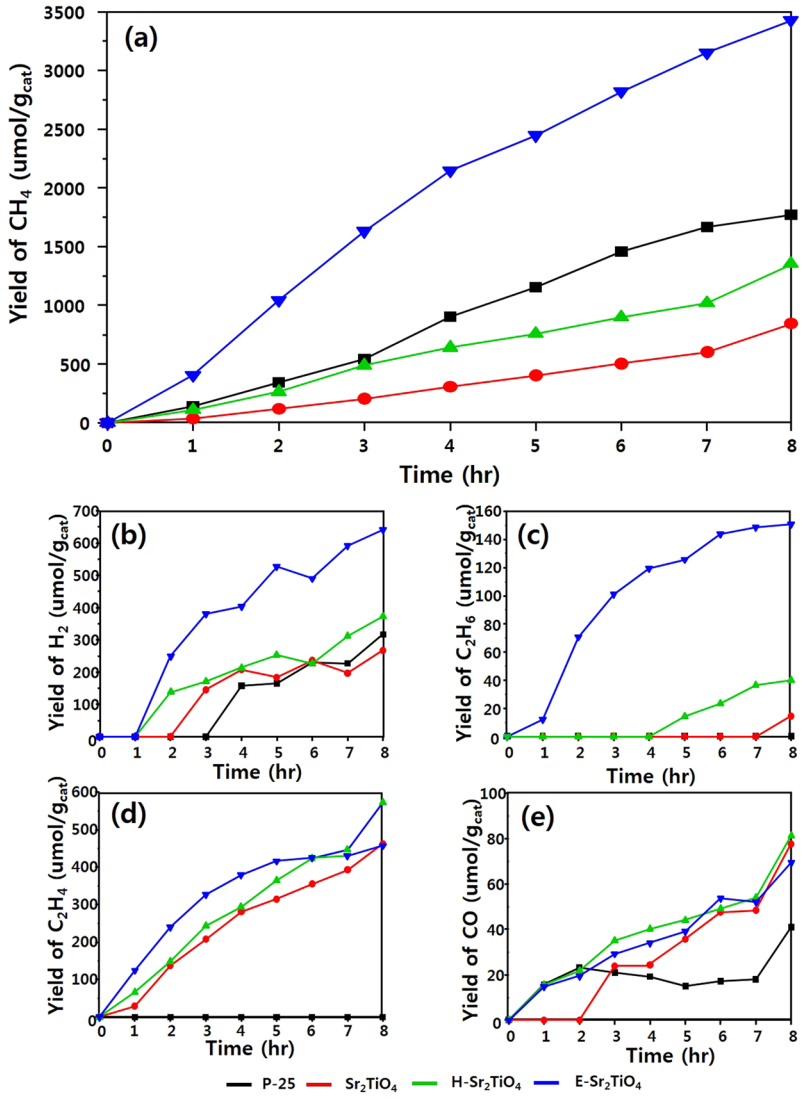

Figure 12. Photocatalytic CO_2 reduction with H_2O on catalysts. (**a**) yield of CH_4, (**b**) yield of H_2 (**c**) yield of C_2H_6 (**d**) yield of C_2H_4, and (**b**) yield of CO.

Therefore, the degree of colloidal dispersion in the solution after CO_2 bubbling follows the order E-Sr_2TiO_4 > P-25 > H-Sr_2TiO_4 > Sr_2TiO_4. Thus, E-Sr_2TiO_4, P-25, and H-Sr_2TiO_4 show good dispersion under the reaction conditions, which is considered advantageous for CO_2 photoreduction performance. However, in the case of Sr_2TiO_4, the zeta potential is low, so it is likely to exhibit poor catalytic performance owing to it being more agglomerated than the other catalysts.

Photocatalytic reduction of CO_2 with H_2O, property after reaction, and mechanism. The products obtained though CO_2 reduction using the catalysts synthesized in this study are CH_4, H_2, C_2H_6, C_2H_4, and CO. Figure 12 shows the accumulation of the products according to irradiation time. The main product is CH_4 and the product amounts follow the order $CH_4 > C_2H_6 > H_2 > C_2H_4 > CO$. Overall, the reactivity of the surface-treated H-Sr_2TiO_4 and E-Sr_2TiO_4 is better than that of Sr_2TiO_4. After 8 h reaction, the rates of CH_4 production over Sr_2TiO_4, H-Sr_2TiO_4, and E-Sr_2TiO_4 are 844.94, 1353.46, and 3431.77 μmol/g_{cat}, respectively. In

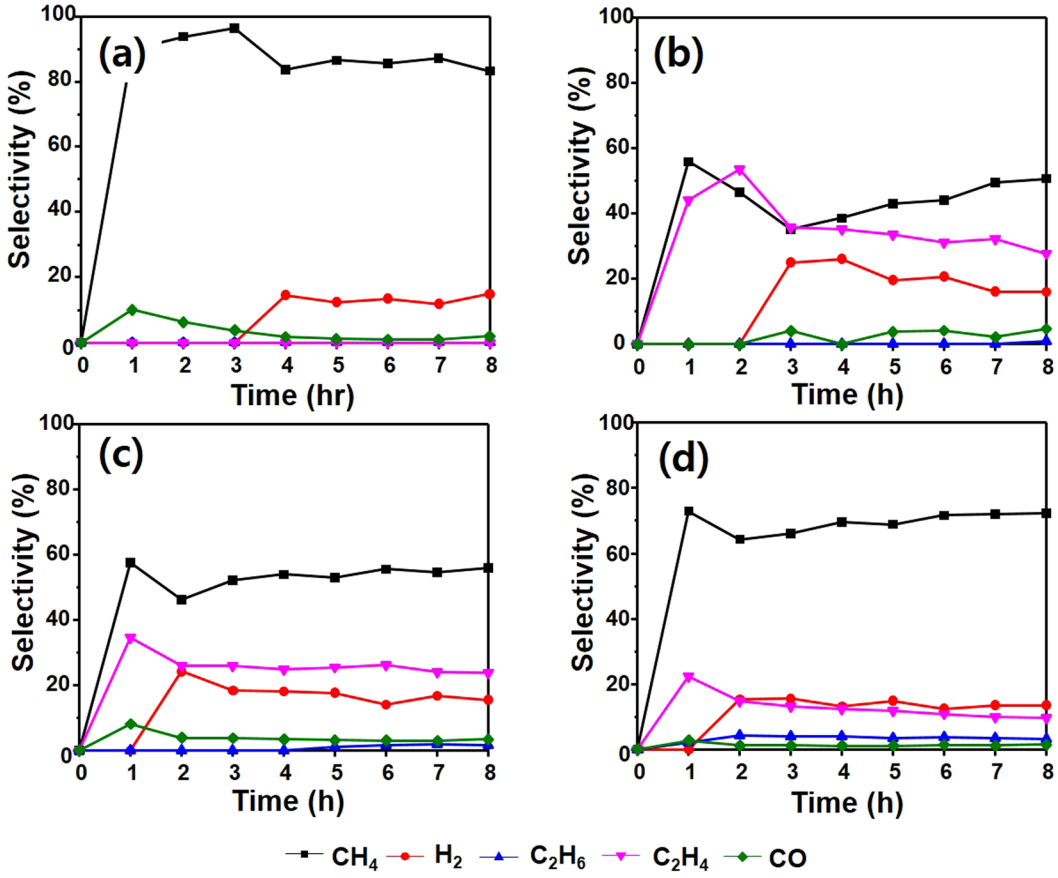

Figure 13. Product distribution on catalysts. (**a**) P-25, (**b**) Sr_2TiO_4, (**c**) H-Sr_2TiO_4 and (**d**) E-Sr_2TiO_4.

Catalysts	Quantum yield (%)					
	CH_4	H_2	C_2H_6	C_2H_4	CO	Total
P-25	2.693	0.120	0.000	0.000	0.016	2.829
Sr_2TiO_4	1.283	0.102	0.019	0.527	0.030	1.961
H-Sr_2TiO_4	2.055	0.142	0.053	0.653	0.031	2.934
E-Sr_2TiO_4	5.211	0.243	0.200	0.521	0.026	6.201

Table 3. The apparent quantum yield of catalysts.

particular, E-Sr_2TiO_4 shows excellent reactivity and produces more CH_4 than P-25 catalyst, and. Figure 12b shows the amounts of H_2 produced. H_2 is a necessary substance for reducing CO_2. Therefore, the greater the amount of H_2 generated, the easier the CO_2 reduction. The amounts of H_2 generated over Sr_2TiO_4, H-Sr_2TiO_4, and E-Sr_2TiO_4 are 267.73, 373.65, and 640.71 $\mu mol/g_{cat}$, respectively. Therefore, the CO_2 reduction reaction is promoted over E-Sr_2TiO_4 is higher than the other catalysts. Furthermore, the C_2H_6 production over E-Sr_2TiO_4 is higher than that over the other catalysts. When E-Sr_2TiO_4 is used, the amount of C_2H_6 produced after 8 h is 150.8 $\mu mol/g_{cat}$. If the C_2H_6 reacts with H_2 on the catalysts surface it can be further converted to CH_4. The amounts of C_2H_4 and CO produced over the catalysts are similar. After 8 h, the production of C_2H_4 and CO is 457.63–573.33 and 69.35–81.30 $\mu mol/g_{cat}$, respectively. Figure 13 shows the product distribution on the catalysts. P-25 showed the highest CH_4 selectivity, which was 80 to 90%. Next, when E-Sr_2TiO_4 was used, the CH_4 selectivity was high and its value was about 70%. Table 3 shows the quantum yield of the catalysts and the overall quantum yield was in the order of E-Sr_2TiO_4, P-25, H-Sr_2TiO_4, and Sr_2TiO_4, which were 2.83, 1.96, 2.93, and 6.20%, respectively. The quantum yield for CO_2 photoreduction to produce CH_4 of P-25, Sr_2TiO_4, H-Sr_2TiO_4 and E-Sr_2TiO_4 were 2.69, 1.28, 2.56, 5.21%, respectively. The quantum yield for other products was less than 1% for all catalysts.

The XRD analysis of the catalysts after the reaction was carried out to confirm the structural stability and displayed in Fig. 14. From the XRD analysis results, it was observed that the catalysts structure was remained stable before and after the reaction. Therefore, the catalysts structure was stable during the reaction conditions.

The photoreaction of E-Sr_2TiO_4 showing the best activity was repeated three times. The results for CH_4 production, the main product, are shown in Fig. 15. A slight amount of difference was observed in the results but

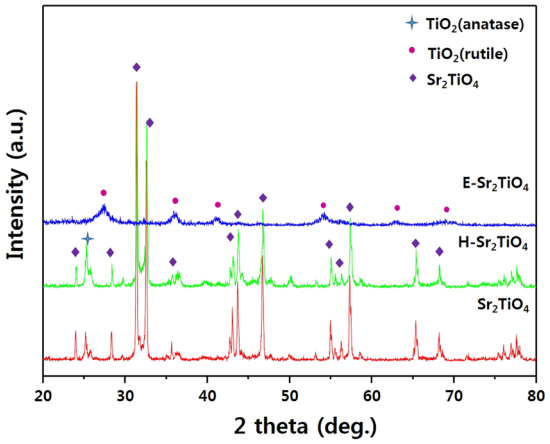

Figure 14. XRD patterns of the Sr_2TiO_4, H-Sr_2TiO_4, and E-Sr_2TiO_4 after the reaction.

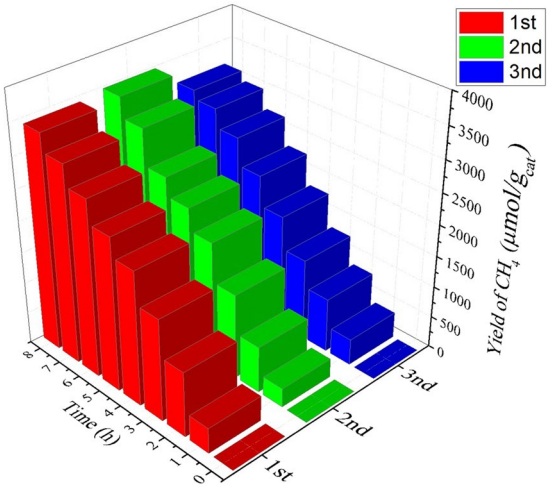

Figure 15. Reusability test of E-Sr_2TiO_4 to convert from CO_2 to CH_4 using photoreduction.

similar performance was maintained without deactivation in all three times. Therefore, it was confirmed that the E-Sr_2TiO_4 was excellent in not only structural stability but also reusability during the reaction

Based on these results, a plausible reaction pathway over E-Sr_2TiO_4, which has the best performance is proposed in Fig. 16. The excited electrons on the exfoliated improved catalyst surface react with CO_2 to produce $\cdot CO_2^-$ radicals, and the holes react with H_2O to produce OH^- and H^+. Hydrogen radicals (·H) are formed by the reaction of H^+ with excited electrons, and then CO is produced by the reaction of ·H and $\cdot CO_2^-$ radicals. CH_4, C_2H_6, and C_2H_4 are produced finally as the CO and ·H radicals continuously react.

Conclusion

In this study, nanosized layered perovskite Sr_2TiO_4 photocatalyst was successfully synthesized by using sol-gel technique with the assistance of citric acid. The surface of layered perovskite Sr_2TiO_4 photocatalyst was treated to improve the CO_2 photoreduction activity. The particles were treated with HNO_3 to remove the Sr ions present between the layers, and the layers were exfoliated by treatment with TPAOH. The catalyst, E-Sr_2TiO_4 showed the rutile TiO_2 structure after exfoliation because the Sr_2TiO_4 structure was collapsed. The shape of the exfoliated thin film was confirmed by TEM. In comparison to Sr_2TiO_4 and H-Sr_2TiO_4 photocatalysts, the exfoliated catalyst E-Sr_2TiO_4 showed an excellent performance in CO_2 photoreduction to CH_4, and after 8 h, 3431.77 $\mu mol/g_{cat}$ of CH_4 was generated. The reason for the excellent performance of E-Sr_2TiO_4 can be explained by the following factors.

First, it has a narrow band gap compared to the other two catalysts, and exhibits reduced electron-hole recombination. Therefore, a relatively larger number of electrons and holes transferred to CO_2 and H_2O. Next, a large amount of CO_2 and H_2O can interact with the active sites on the surface because it has a large surface area and is well dispersed in the solution. Based on the excellent physical and photochemical properties of the exfoliated layered perovskite catalyst, it may be employed for different photocatalytic applications as well as the CO_2 photoreduction reactions.

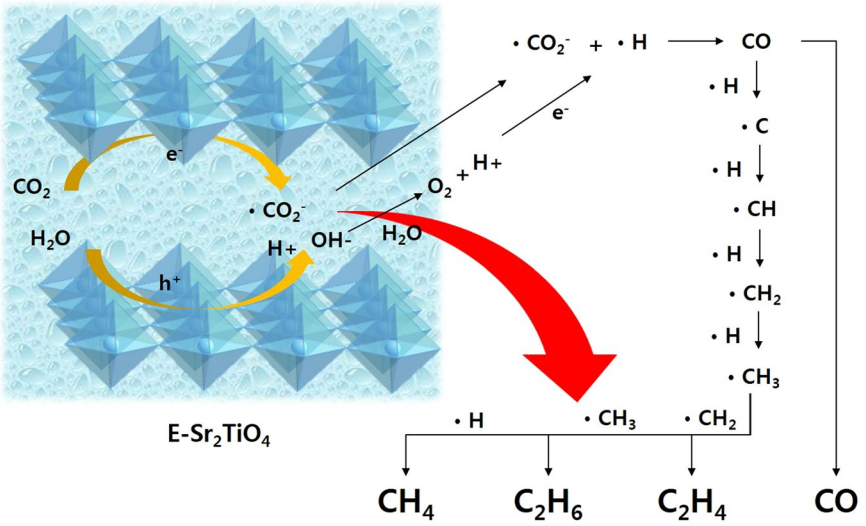

Figure 16. The proposed mechanism for the photo-reduction of CO_2 with H_2O on E-Sr_2TiO_4.

Methods

Synthesis of photocatalysts. The synthesis of layered perovskite Sr_2TiO_4 was performed as follows: Strontium nitrate ($Sr(NO_3)_2$, 97.0%, Junsei Chemical, Japan) and titanium isopropoxide ($Ti(OCH(CH_3)_2)_4$, TTIP, 98.0%, Junsei Chemical, Japan) were used as precursors. First, 0.1 mol of $Sr(NO_3)_2$ was dissolved in double distilled water (100 mL) with continuous stirring. Then, 10 mL of HNO_3 (60%, OCI company Ltd., Republic of Korea) was added with stirring to prevent hydrolysis. This solution was labeled A. In a separate vessel, 0.05 mol of TTIP was dissolved in EtOH (99.9%, OCI company Ltd., Republic of Korea), and then glacial acetic acid (CH_3COOH, 99.0%, Ducsan, Republic of Korea) was added with stirring to prevent hydrolysis. This solution was labeled as B. The solutions A and B were then mixed with stirring, and citric acid monohydrate ($C_6H_8O_7{\cdot}H_2O$, 99.5%, Daejung Chemicals and Metals Co Ltd., Republic of Korea), which is a complexing agent for the gel, was added, and the mixture was stirred until it became homogeneous. Then, the solvent was removed without the temperature exceeding 323.15 K to obtain a sol gel, which was subsequently pretreated at 493.15 K. Finally, a white powder was obtained by thermal treatment at 1323.15 K for 6 h. In some cases, hydrogen treatment was then performed at 1123.15 K for 3 h in H_2 atmosphere. In other cases, exfoliation was achieved by a three-step process, as shown in Fig. 17. Ion exchange of Sr for H cations was carried out in 1 M HNO_3 for 5 days using ultrasonication. The powder obtained was treated in tetrapropylammonium hydroxide (TPAOH, 25.0%, in water, ACROS, Belgium) for 3 weeks using ultrasonication. The final white precipitate was washed several times with distilled water and ethanol and dried at 343 K for 24 h. The hydrogen-treated and exfoliated Sr_2TiO_4 samples were labeled H-Sr_2TiO_4 and E-Sr_2TiO_4, respectively.

Characterization of photocatalysts. The structures and crystallinities of the as-prepared Sr_2TiO_4, H-Sr_2TiO_4, and E-Sr_2TiO_4 samples were confirmed with XRD (model MPD from PANalytical) using nickel-filtered CuKα radiation (40.0 kV, 30.0 mA). The morphologies were investigated using HR-TEM (Tecnal G2 F20 S-TWIN, FEI, Netherlands) operated at 200 kV. The presence of different elements was confirmed using the elemental mapping and energy dispersive X-ray spectroscopy (EDS) attached to the TEM setup. The specific surface areas (S_{BET}) were calculated according to the Brunauer-Emmett-Teller theory using a Belsorp II mini (BEL, Japan Inc.). The UV-Vis absorption spectra were obtained using a SCINCO Neosys-2000 spectrometer fitted with a reflectance sphere. PL profiles were obtained using a SCINCO FluoroMate FS-2 at room temperature using a He-Cd laser source at a wavelength of 325 nm. XPS measurements were performed on a K-alpha (Thermo Scientific, UK) using Al Kα X-rays as the excitation source. The zeta potential of the material was determined by electrophoretic mobility using an electrophoresis measurement apparatus (ELS 8000, Otsuka Electronics, Japan) with a plate sample cell. Electrophoretic light scattering (ELS) determination was performed in reference beam mode with a 670 nm laser light source at a modular frequency of 250 Hz and a scattering angle of 15°. The standard error of the zeta potential, converted from the experimentally determined electrophoretic mobility, was typically $<$1.5% with 5% error. To measure the zeta potentials, the samples were dispersed in deionized water or bubbling-CO_2 water at 0.1 wt%. The final zeta potentials were obtained by averaging 2 or 3 measurements.

Photocatalytic activity measurements. The photocatalytic tests for the reduction of CO_2 with H_2O were performed in a photoreactor comprising a quartz chamber with a total volume of 150.0 cm^3 (Fig. 18). To photoreduce CO_2, 0.01 g of the catalyst was placed in the reactor chamber with 50 mL of double distilled water, and the reactor was closed. A UV lamp (6 W/cm^2, 20 cm length × 2.0 cm diameter, Shinan, Republic of Korea) emitting light at 365 nm was used to irradiate the reaction mixture. Supercritical-fluid-grade CO_2 with a certified maximum hydrocarbon content of $<$1 ppm was used as the reactant. Before the reaction was initiated by illumination, the reactor was purged with CO_2 gas for 5 min. The lamp was then switched on to start the experiment. The reaction temperature and pressure were maintained at 303 K and 1 atm, respectively. The gas products were

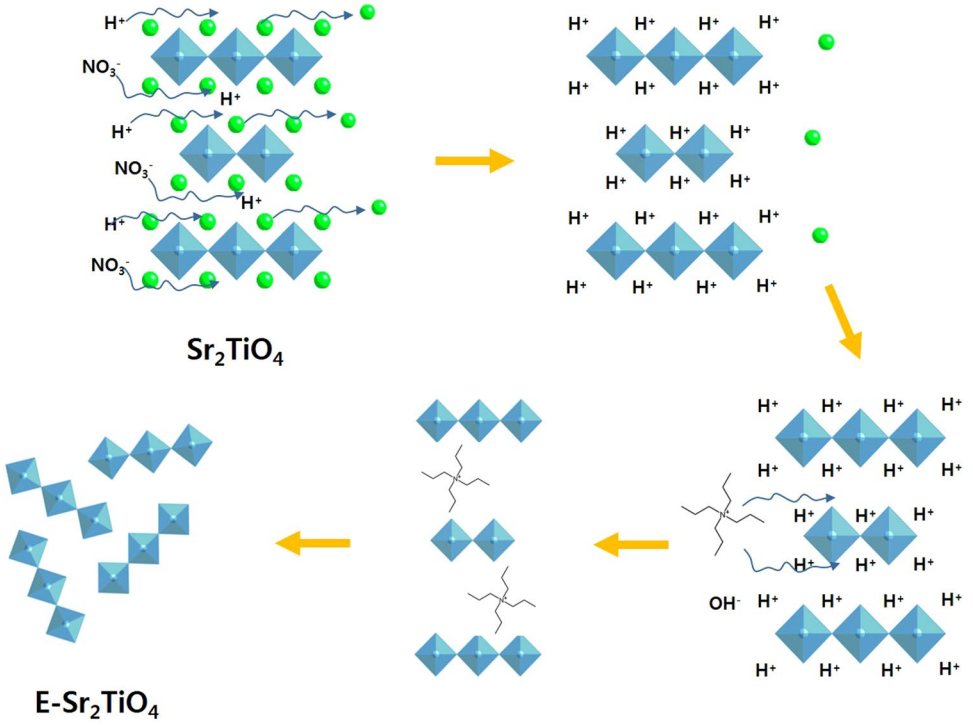

Figure 17. Preparation of Sr_2TiO_4, Exfoliation Sr_2TiO_4 and H-Sr_2TiO_4 catalysts.

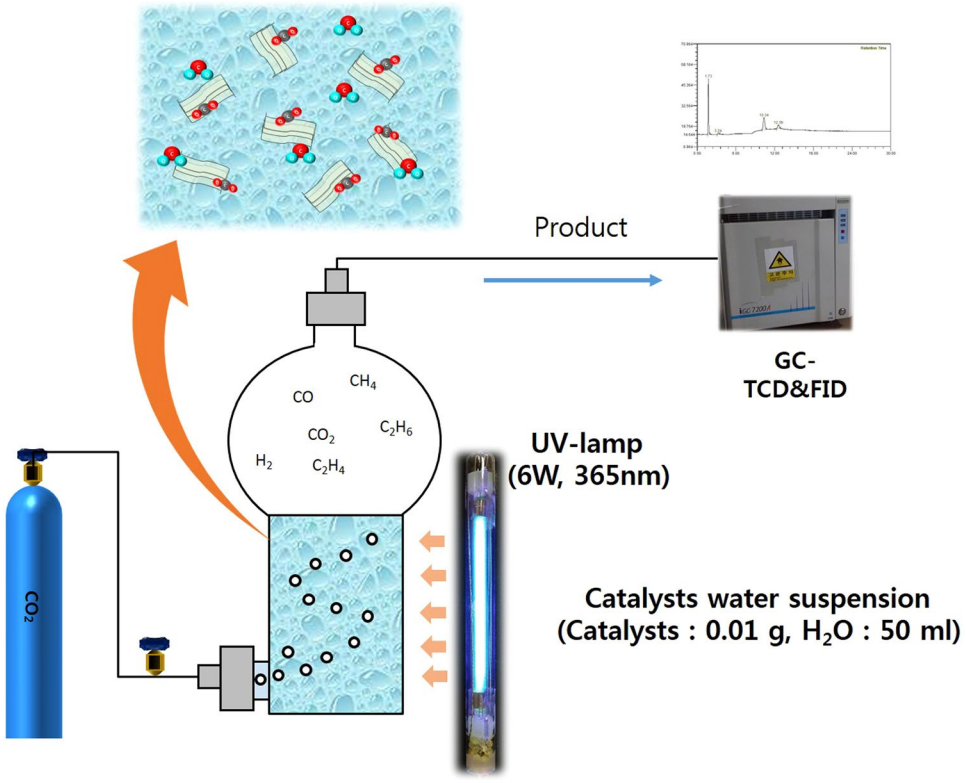

Figure 18. The Schematic diagram of experimental set up of a circulated photo reactor for CO_2 reduction.

analyzed using a gas chromatograph (iGC7200, DS Science, Republic of Korea) equipped with a thermal conductivity detector (TCD) and a flame ionization detector (FID). The product yield[33] and quantum yield[63] during reaction was calculated using following equation (2–3).

$$\text{Product yield} = \text{Total of product } (\mu\text{mol})/\text{Amount of photocatalyst used}(g_{cat}) \quad (2)$$

$$\text{Quantum yield}(\%) = \text{Number of reacted electrons/Number of incident photons} \times 100\% \quad (3)$$

References

1. Dewi, M. S., Hartono, D. M., Moersidik, S. S. & Kustiwan, I. Green housing evaluation through carbon footprint dynamic model: questioned the urban policy sustainability. Procedia Soc. *Behav Sci.* **227**, 317–324 (2016).
2. Najafi-Marghmaleki, A., Barati-Harooni, A. & Mohammadi, A. Impact of gas impurities on CO_2 mole fraction: Application in carboncapture and storage (CCS) processes. *Int. J. Greenhouse Gas Control.* **57**, 173–184 (2017).
3. Mechleri, E., Brown, S., Fennell, P. S. & Dowell, N. M. CO_2 capture and storage (CCS) cost reduction viainfrastructure right-sizing. *Chem. Eng. Res. Des.* **119**, 130–139 (2017).
4. Oh, S. T. & Martin, A. Thermodynamic efficiency of carbon capture and utilisation in anaerobic batch digestion process. *J. CO2 Util.* **16**, 182–193 (2016).
5. Kang., D. *et al*. Carbon capture and utilization using industrial wastewater under ambient conditions. *Chem. Eng. J.* **308**, 1073–1080 (2017).
6. Pan, S. –Y., Lafuente, A. M. L. & Chiang, P. –C. Engineering, environmental and economic performance evaluation of high-gravity carbonation process for carbon capture and utilization. *Appl. Energy* **170**, 269–277 (2016).
7. Li, X. *et al*. Engineering heterogeneous semiconductors for solar water splitting. *J. Mater. Chem. A* **3**, 2485–2534 (2015).
8. Enoue, T., Fujishima, A., Konishi, S. & Honda, K. Photoelectrocatalytic reduction of carbon dioxide in aqueous suspensions of semiconductor powders. *Nature* **277**, 637–638 (1979).
9. Chen, L. *et al*. Photoreduction of CO_2 by TiO_2 nanocomposites synthesized through reactive direct current magnetron sputter deposition. *Thin Solid Films* **517**, 5641–5645 (2009).
10. Wang, P. –Q., Bai, Y., Luo, P. –Y. & Liu, J. –Y. Graphene–WO_3 nanobelt composite: Elevated conduction band toward photocatalytic reduction of CO_2 into hydrocarbon fuels. *Catal. Commun.* **38**, 82–85 (2013).
11. Li, X. *et al*. Green synthesis and photo-catalytic performances for ZnO-reduced graphene oxide nanocomposites. *J. Colloid Interface Sci.* **411**, 69–75 (2013).
12. Marcì, G., Garía-López, E. I. & Palmisano, L. Photocatalytic CO_2 reduction in gas–solid regime in the presence of H_2O by using GaP/TiO_2 composite as photocatalyst under simulated solar light. *Catal. Commun.* **53**, 38–41 (2014).
13. Beigi, A. A., Fatemi, S. & Salehi, Z. Synthesis of nanocomposite CdS/TiO_2 and investigation of its photocatalytic activity for CO_2 reduction to CO and CH_4 under visible light irradiation. *J. CO2 Util.* **7**, 23–29 (2014).
14. Li, H. *et al*. Photocatalytic reduction of carbon dioxide to methanol by Cu_2O/SiC nanocrystallite under visible light irradiation. *J. Nat. Gas Chem.* **20**, 145–150 (2011).
15. Zhao, C., Krall, A., Zhao, H., Zhang, Q. & Li, Y. Ultrasonic spray pyrolysis synthesis of Ag/TiO_2 nanocomposite photocatalysts for simultaneous H_2 production and CO_2 reduction. *Int. J. Hydrogen Energy* **37**, 9967–9976 (2012).
16. Wang, W. –N. *et al*. Size and Structure Matter: Enhanced CO_2 Photoreduction Efficiency by Size-Resolved Ultrafine Pt Nanoparticles on TiO2 Single Crystals. *J. Am. Chem. Soc.* **134**, 11276–11281 (2012).
17. Lee, C. –W. *et al*. Photocatalytic conversion of CO_2 to hydrocarbons by light-harvesting complex assisted Rh-doped TiO_2 photocatalyst. *J. CO2 Util.* **5**, 33–40 (2014).
18. Zbudniewek, K., Góralski, J. & Rynkowski, J. Studies on TiO_2/SiO_2 and Pd/TiO_2/SiO_2 Catalysts in Photoreduction of CO_2 with H_2O to Methanol1. *Russ. J. Phys. Chem. A* **86**, 2057–2062 (2012).
19. Kwak, B. S. *et al*. Methane formation from photoreduction of CO_2 with water using TiO_2 cluding Ni ingredient. *Fuel* **143**, 570–576 (2015).
20. Tseng, I. –H., Wu, J. C. S. & Chou, H. –Y. Effects of sol–gel procedures on the photocatalysis of Cu/TiO_2in CO_2 photoreduction. *J. Catal.* **221**, 432–440 (2004).
21. Park, M., Kwak, B. S., Jo, S. W. & Kang, M. Effective CH_4 production from CO_2 photoreduction using TiO_2/x mol% Cu–TiO_2 double-layered films. *Energy Convers. Manage.* **103**, 431–438 (2015).
22. Abdullah, H., Khan, M. R., Pudukudy, M., Yaakob, Z. & Ismail, N. A. CeO_2-TiO_2 as a visible light active catalyst for the photoreduction of CO_2 to methanol. *J. Rare Earths* **33**, 1155–1161 (2015).
23. Wang, F., Zhou, Y., Li, P., Kuai, L. & Zou, Z. Synthesis of bionic-macro/microporous MgO-modified TiO_2 for enhanced CO_2 photoreduction into hydrocarbon fuels. *Chin. J. Catal.* **37**, 863–868 (2016).
24. Tahir, M. & Amin, N. S. Performance analysis of nanostructured NiO–In_2O_3/TiO_2 catalyst for CO_2 photoreduction with H_2 in a monolith photoreactor. *Chem. Eng. J.* **285**, 635–649 (2016).
25. Lee, H. *et al*. Assembly of a check-patterned CuS_x–TiO_2 film with an electron-rich pool and its application for the photoreduction of carbon dioxide to methane. *Appl. Surf. Sci.* **393**, 385–396 (2017).
26. Lee, J. H., Kim, S.-I., Park, S.-M. & Kang, M. A p-n heterojunction NiS-sensitized TiO_2 photocatalytic system for efficient photoreduction of carbon dioxide to methane. *Ceram. Int.* **43**, 1768–1774 (2017).
27. Tahir, M., Tahir, B., Amin, N. A. S. & Alias, H. Selective photocatalytic reduction of CO_2 by H_2O/H_2 to CH_4 and CH_3OH over Cu-promoted In_2O_3/TiO_2 nanocatalyst. *Appl. Surf. Sci.* **389**, 46–55 (2016).
28. Do, J. Y., Im, Y., Kwak, B. S., Kim, J. –Y. & Kang, M. Dramatic CO_2 photoreduction with H_2O vapors for CH_4 production using the TiO_2 (bottom)/Fe–TiO_2 (top) double-layered films. *Chem. Eng. J.* **275**, 288–297 (2015).
29. Gui, M. M., Chai, S. –P. & Mohamed, A. R. Modification of MWCNT@TiO_2 core–shell nanocomposites with transition metal oxide dopants for photoreduction of carbon dioxide into methane. *Appl. Surf. Sci.* **319**, 37–43 (2014).
30. Zhou, M., Hou, Z. & Chen, X. The Effects of Hydrogenation on Graphitic C_3N_4 Nanosheets for Enhanced Photocatalytic Activity. *Part. Part. Syst. Charact.* **2017**, 1700038–1700046 (2017).
31. Zeng, D. *et al*. $Ni_{12}P_5$ nanoparticles embedded into porous g-C_3N_4 nanosheets as a noble-metal-free hetero-structure photocatalyst for efficient H2 production under visible light. *J. Mater. Chem. A*, https://doi.org/10.1039/C7TA04816E (2017).
32. Chen, W. *et al*. Synergetic enhancement of plasmonic hot-electron injection in Au cluster-nanoparticle/C_3N_4 for photocatalytic hydrogen evolution. *J. Mater, Chem. A*, https://doi.org/10.1039/C7TA03808A (2017).
33. Ong, W.-J., Putri, L. K., Tan, L.-L., Chai, S.-P. & Yong, S.-T. Hetrostructured AgX/g-C_3N_4 (X = Cl and Br) nanocomposites via a sonication-assisted deposition-precipitation approach: Emerging role of halide ions in the synergistic photocatalytic reduction of carbon dioxide. *Appl. Catal., B* **180**, 530–543 (2016).
34. Kuriki, R. *et al*. Robust Binding between Carbon Nitride Nanosheets and a binuclear Ruthenium (II) Complex Enabling Durable, Selective CO_2 Reduction under Visible Light in Aqueous Solution. *Angew. Chem. Int. Ed.* **56**, 4867–4871 (2017).
35. Kuriki, R. *et al*. Nature-Inspired, Highly Durable CO_2 Reduction System Consisting of a Binuclear Ruthenium(II) Complex and an Organic Semiconductor Using Visible Light. *J. Am. Chem. Soc.* **138**, 5159–5170 (2016).
36. Ong, W.-J. *et al*. Unraveling charge carrier dynamics in protonated g-C_3N_4 interfaced with carbon nano dots as co-catalysts toward enhanced photocatalytic CO_2 reduction: A combined experimental and first-principles DFT study. *Nano Res.* **10**, 1673–1676 (2017).

37. Ong, W.-J., Tan, L.-L., Ng, Y. H., Yong, S.-T. & Chai, S.-P. Graphitic Carbon Nitride (g-C_3N_4)-Based Photocatalysts for Artificial Photosynthesis and Environmental Remediation: Are We a Step Closer To Achieving Sustainability? *Chem. Rev.* **116**, 7159–7329 (2016).
38. Wang, S., Yao, W., Lin, J., Ding, Z. & Wang, X. Cobalt Imidazolate Metal-Organic Frameworks Photosplit CO_2 under Mild Reaction Conditions. *Angew. Chem. Int. Ed.* **53**, 1034–1038 (2014).
39. Wang, S. & Wang, X. Imidazolium Ionic Liquids, Imidazolylidene Heterocyclic Carbenes, and Zeolitic Imidazolate Frameworks for CO_2 Capture and Photochemical Reduction. *Angew. Chem. Int. Ed.* **55**, 2308–2320 (2016).
40. Wang, S. & Wang, X. Multifunctional Metal-Organic Frameworks for Photocatalysis. *Small* **11**, 3097–3112 (2015).
41. Wang, S. & Wang, X. Photocatalytic CO_2 reduction by CdS promoted with a zeolitic imidazolate framework. *Appl. Catal., B* **162**, 494–500 (2015).
42. Wu, G. *et al*. Hydrothermal synthesis and visible-light-driven photocatalytic degradation for tetracycline of Mn-doped $SrTiO_3$ nanocubes. *Appl. Surf. Sci.* **333**, 39–47 (2015).
43. Bui, D.-N., Mu, J., Wang, L., Kang, S.-Z. & Li, X. Preparation of Cu-loaded $SrTiO_3$ nanoparticles and their photocatalytic activity for hydrogen evolution from methanol aqueous solution. *Appl. Surf. Sci.* **274**, 328–333 (2013).
44. Ruzimuradov, O. *et al*. A facile preparation of dual-phase nitrogen-doped TiO_2–$SrTiO_3$ macroporous monolithic photocatalyst for organic dye photodegradation under visible light. *J. Eur. Ceram. Soc.* **35**, 1815–1821 (2015).
45. Zhang, Z., Liu, G. & Mao, Y. Improved separation efficiency of photogenerated carriers for Fe_2O_3/$SrTiO_3$ heterojunction Semiconductor. *Int. J. Hydrogen Energy* **38**, 9349–9354 (2013).
46. Kang, H. W., Park, S. B., Kim, J. G. & Kim, I. T. Effects of F for enhancement of H_2 evolution on visible-light-driven photocatalyst of $SrTiO_3$:Cr/Ta/F prepared by spray pyrolysis. *Int. J. Hydrogen Energy* **39**, 5537–5545 (2014).
47. Zhang, W., Du, L., Bi, F. & He, H. A novel $SrTiO_3$/HZSM-5 photocatalyst prepared by sol–gel method. *Mater. Lett.* **157**, 103–105 (2015).
48. Liu, Y. *et al*. Sandwich $SrTiO_3$/TiO_2/H-Titanate nanofiber composite photocatalysts for efficient photocatalytic hydrogen evolution. *Appl. Surf. Sci.* **315**, 314–322 (2014).
49. Niishiro, R., Tanaka, S. & Kudo, A. Hydrothermal-synthesized $SrTiO_3$ photocatalyst codoped with rhodium and antimony with visible-light response for sacrificial H_2 and O_2 evolution and application to overall water splitting. *Appl. Catal. B* **150–151**, 187–196 (2014).
50. Shen, S., Jia, Y., Fan, F., Feng, Z. & Li, C. Time-resolved infrared spectroscopic investigation of roles of valence states of Cr in (La,Cr)-doped $SrTiO_3$ photocatalysts. *Chin. J. Catal.* **34**, 2036–2040 (2013).
51. Hirayama, J., Abe, R. & Kamiya, Y. Combinational effect of Pt/$SrTiO_3$:Rh photocatalyst and SnPd/Al_2O_3 non-photocatalyst for photocatalytic reduction of nitrate to nitrogen in water under visible light irradiation. *Appl. Catal. B* **144**, 721–729 (2014).
52. Zou, J.-P. *et al*. Preparation and photocatalytic activities of two new Zn-doped $SrTiO_3$ and $BaTiO_3$ photocatalysts for hydrogen production from water without cocatalysts loading. *Int. J. Hydrogen Energy* **37**, 17068–17077 (2012).
53. Guo, J. *et al*. A new heterojunction Ag_3PO_4/Cr-$SrTiO_3$ photocatalyst towards efficient elimination of gaseous organic pollutants under visible light irradiation. *Appl. Catal. B* **134–135**, 286–292 (2013).
54. Kang, H. W., Lim, S. N., Song, D. & Park, S. B. Organic-inorganic composite of g-C_3N_4-$SrTiO_3$:Rh photocatalyst for improved H_2 evolution under visible light Irradiation. *Int. J. Hydrogen Energy* **37**, 11602–11610 (2012).
55. Kwak, B. S. & Kang, M. Photocatalytic reduction of CO_2 with H_2O using perovskite $Ca_xTi_yO_3$. *Appl. Surf. Sci.* **337**, 138–144 (2015).
56. Do, J. Y., Im, Y., Kwak, B. S., Park, S. –M. & Kang, M. Preparation of basalt fiber@perovskite $PbTiO_3$ core–shell composites and theireffectsonCH4 production fromCO2 photoreduction. *Ceram. Int.* **42**, 5942–5951 (2016).
57. Sun, X. & Xu, X. Efficient photocatalytic hydrogen production over La/Rh co-doped Ruddlesden-Popper compound Sr_2TiO_4. *Appl. Catal. B* **210**, 149–159 (2017).
58. Zak, A. K., Majid, W. H. A., Abrishami, M. E., Yousefi, R. & Parvizi, R. Synthesis, magnetic properties and X-ray analysis of $Zn_{0.97}X_{0.03}O$ nanoparticles (X = Mn, Ni, and Co) using Scherrer and size-strain plot methods. *Solide State Sci.* **14**, 488–494 (2012).
59. Yu, Q. *et al*. Different toxicity of anatase and rutile TiO_2 nanoparticles on macrophages: Involvement of difference in affinity to proteins and phospholipids. *J. Hazard. Mater.* **335**, 125–134 (2017).
60. Khan, I., Ahmad, I., Amin, B., Murtaza, G. & Ali, Z. Bandgap engineering of $Cd_{1-x}Sr_xO$. *Physica B* **406**, 2509–2514 (2011).
61. Tumuluri, A., Naidu, K. L. & Raju, K. C. J. Band gap determination using Tauc's plot for $LiNbO_3$ thin films. *Int J Chemtech Res* **6**, 3353–3356 (2014).
62. Huang, Y. *et al*. Preparation of 2D hydroxyl-rich carbon nitride nanosheets for photocatalytic reduction of CO_2. *RSC adv.* **5**, 33254–33261 (2015).
63. Park, H.-A., Choi, J. H., Choi, K. M., Lee, D. K. & Kang, J. K. Highly porous gallium oxide with a high CO_2 affinity for the photocatalytic conversion of carbon dioxide into methane. *J. Mater. Chem.* **22**, 5304–5307 (2012).

Acknowledgements

This research was supported by Basic Science Research Program through the National Research Foundation of Korea (NRF) funded by the Ministry of the Science ICT & Future Planning (NRF-2015R1A1A3A04001268).

Author Contributions

B.S.K. and M.K. designed the study, performed experiments, analyzed data and wrote the manuscript. J.Y.D. carried out catalytic stability test, N.-K. Park performed XRD analysis of the catalyst after reaction. All authors discussed the results and reviewed the manuscript.

Additional Information

Competing Interests: The authors declare that they have no competing interests.

Publisher's note: Springer Nature remains neutral with regard to jurisdictional claims in published maps and institutional affiliations.